metals

MDPI

Article

Percolating Ta/Nb-Al_2O_3 Refractory Composites via Spark Plasma Sintering

Gregory Kallien [1,*], Susanne Wagner [1] and Karl Günter Schell [1,2]

[1] Institute for Applied Materials—Ceramic Materials and Technologies (IAM-KWT), Karlsruhe Institute of Technology (KIT), 76131 Karlsruhe, Germany
[2] Prüf- und Forschungsinstitut Pirmasens e.V. (PFI), Marie-Curie-Straße 19, 66953 Pirmasens, Germany
* Correspondence: gregory.kallien@kit.edu

Abstract

The electrification of high-temperature industrial processes requires refractory materials that combine thermal stability with tailored electrical functionality. In this study, Ta/Nb-Al_2O_3 composites were prepared by spark plasma sintering (SPS) to investigate densification, metal-phase deformation, electrical conductivity and percolation behavior. Coarse, fine and superfine alumina powders were combined with tantalum or niobium and sintered at 1300–1600 °C for 5 min with 50 MPa uniaxial pressure. The results show that the alumina particle size and morphology strongly influence the formation of conductive metal networks. Coarse alumina promotes deformation and elongation of the metallic phase, thereby improving metal-phase connectivity and lowering the operational percolation threshold. Fine and superfine alumina enhance densification but can delay percolation by embedding metal particles in a dense ceramic matrix. Combining these fractions, both effects can be balanced, enabling improved densification while maintaining effective conductive pathways. An operational percolation threshold of 7.5 vol.-% was obtained for Ta/coarse alumina, indicating highly effective metal-phase connectivity after SPS. Microstructural analysis supports the interpretation that matrix-controlled metal-particle deformation and spatial distribution govern the electrical response. Tailored alumina matrix design can reduce the refractory metal content required for conductive ceramic–metal composites.

Keywords: spark plasma sintering; refractory composites; percolation theory; particle size; densification; electrical conductivity; µCT; circularity

1. Introduction

Global energy supply continues to be predominantly reliant on fossil fuels. Despite the advanced shift to renewable sources, the challenges associated with this transition are visible in multiple dimensions. Because high-temperature industrial processes account for substantial energy consumption, their electrification requires materials that can withstand harsh thermal environments while providing tailored electrical functionality [1]. Recent work on conductive ceramic composites for high-temperature thermal energy storage further demonstrates the relevance of microstructural designs that combine thermal stability with controlled electrical functionality [2]. The combination of advanced processing methodologies and specified raw materials with regard to shape and particle size distribution offers novel approaches for optimized material characteristics and properties. Spark plasma sintering (SPS) is a pressure-assisted sintering technique in which pulsed electric current and uniaxial pressure are used to promote densification [3–5].

Academic Editor: Eric Hug

Received: 29 May 2026
Revised: 29 June 2026
Accepted: 30 June 2026
Published: 5 July 2026

https://doi.org/10.3390/met16070742

The process is known, among other things, for its ability to process fine-grained materials and limit grain growth due to its minimal dwell times and rapid heating rates. The present approach uses SPS to enhance densification, modify the aspect ratio of the refractory metal phase and promote the formation of an interconnected conductive network [6–8]. Recent SPS work on tantalum-containing alumina–zirconia ceramic–metal composites further demonstrates the current relevance of refractory-metal reinforcement in oxide ceramic matrices and highlights the role of metal-particle distribution for mechanical performance [9]. As demonstrated in the study, the alumina particle size and morphology strongly affect both densification and the formation of conductive metal networks. The results show that a tailored alumina matrix composition can reduce the operational percolation threshold by promoting metal-phase connectivity, thereby reducing the costs for economic processing of such materials.

This work addresses the first step of a two-step processing route aimed at producing dense, electrically percolating composite granules for subsequent sintering into refractory components. These granules undergo a second sintering step, resulting in a microscopically dense material with porosity on the macroscale for improving thermal properties and less shrinkage for large volume components.

Our study is part of a larger research project [10–12] focused on the development of coarse-grained, non-shrinking, electrically conductive refractory composite materials produced via a two-cycle sintering process. These materials are intended to provide improved thermal shock resistance after the second sintering cycle, combined with current-based preheatable applications and tools in metallurgy like stoppers and components in gas turbines [13].

Within this collaborative project, the present study focuses on the SPS-based initial processing step, which is used to produce dense and electrically percolating Ta/Nb–Al_2O_3 composites as starting materials for subsequent processing. This step is investigated for composites with metal contents up to 30 vol.-%, SPS temperatures between 1300 and 1600 °C, a dwell time of 5 min and a maximum uniaxial pressure of 50 MPa. Within this processing window, the alumina matrix composition is used to control relative density, metal-phase deformation, anisotropic electrical conductivity and the operational percolation threshold [14,15]. This study includes an investigation of microstructure and its effect on anisotropy, functional properties, densification behavior and the comparison of 3D-based simulation with experimental results.

2. Materials and Methods

2.1. Raw Materials

Three different alumina powders were selected as ceramic matrix materials: alumina CT9FG by Almatis GmbH (Ludwigshafen, Germany), hereafter referred to as CT9FG; Treibacher Alodur WRG (Imery Fused Minerals Zschornewitz GmbH, Gräfenhainichen, Germany), referred to as Alodur; and Martoxid MR 70d (Martinswerk GmbH, Bergheim, Germany), referred to as Martoxid. The refractory metals tantalum (Haines & Maassen Metallhandelsgesellschaft mbH, Bonn, Germany) and niobium (EWG Wagner, Weissach, Germany) were chosen due to their high melting temperatures and similar coefficient of thermal expansion to alumina. The powders were also used in other publications related to the FOR 3010 project. Further XRD investigations have already been performed by [8,14].

Particle size distributions were determined by laser diffraction and dynamic image analysis using a CILAS system and a Bettersizer S3 Plus particle size analyzer (CILAS, Orléans, France).

2.2. Sample Processing

The powders with metal contents between 0 and 30 vol.-% were initially dry-mixed in a Turbular Tumbler T2C (WAB AG, Maschinenfabrik, Basel, Switzerland) and sieved twice with a mesh size of 180 µm (stainless steel, Retsch GmbH, Haan, Germany)) to destroy agglomerates.

The samples (d = 20 mm, height = 4 mm)) were heated with 100 K/min, controlled by pyrometer-based temperature control, and sintered at approximately 10 mbar after two argon flushing cycles at 1300–1600 °C with a dwell time of 5 min (Figure 1) by using a graphite tool setup in a SPS system (HP D 25/1 by FCT Systeme GmbH, Frankenblick, Germany). At the maximum temperature, a uniaxial pressure of 50 MPa was applied.

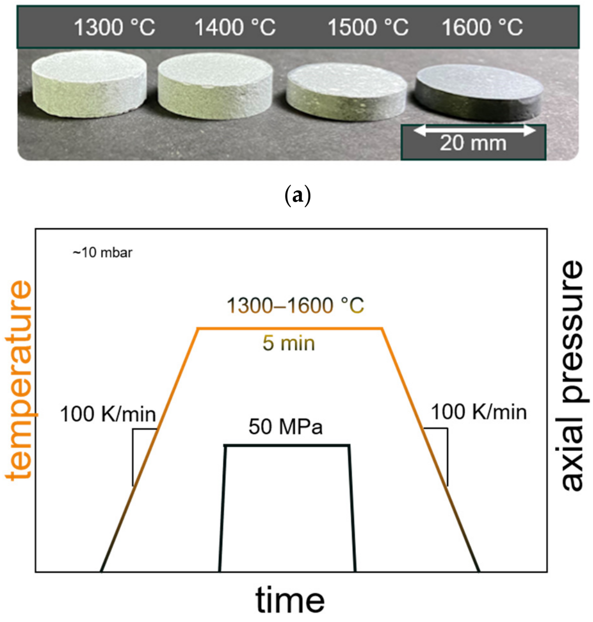

(**a**)

(**b**)

Figure 1. Produced samples at different sintering temperatures (**a**) and SPS parameters (**b**).

For comparison with the conventional sintering route, an Astro graphite furnace (model No. 1000-3560-FP20) with a Stange SE-502 (Stange Elektronik GmbH, Wiehl, Germany) controlling unit was used. The uniaxially pressed green bodies (50 MPa) were sintered for two hours at 1600 °C, while heating up with a ramp of 30 K/min.

2.3. Densification and Electrical Conductivity

The investigation put a focus on sintering behavior, resulting in densification and electrical conductivity depending on sintering parameters, raw materials and metal content (vol.-%). Relative density was measured according to Archimedes' principle by taking the dry mass, the soaked mass and the immersed mass into account.

The electrical measurements were performed with a double-layer electrode. Before applying the electrodes, the samples were ground with SiC-papers (grit size P800) to ensure a plane surface for the electrode. After sputtering the surface using a Quorum Q150T ES (Quorum, Laughton, UK), the surface was covered with a layer of silver paste (Pelco Colloidal, Plano GmbH, Wetzlar, Germany) to ensure the same quality of electrodes regarding the surfaces and roughness of different material compositions.

The electrical conductance was measured in a four-wire configuration using full-area electrodes on both sample faces. Current was applied through the current leads, while the voltage drop across the sample was recorded using separate sense leads. The specific electrical conductivity was calculated from the measured conductance and the sample geometry. By applying current values of 1, 10 and 100 mA with a Keithley 220 Programmable Current Source, the resulting voltage was measured with a Keithley 220 Multimeter to calculate conductance G according to Equation (1)

$$G = \frac{I}{U} \tag{1}$$

and with respect to the geometry, the specific electrical conductivity σ was calculated with Formula (2)

$$\sigma = \frac{G \cdot l}{A} \tag{2}$$

using the conductance G, the distance between both sample faces l and the cross-section area A.

The percolation threshold was defined considering the measurement limits of the experimental setup, which allows conductance values down to 10^{-5} S to be measured. Accordingly, the lowest measurable specific conductivities, depending on the exact geometry of the samples, are between 10^{-6} and 10^{-5} S/cm, which is already in the range of electrical insulators. Non-measurable samples were therefore defined as "non-conductive".

2.4. Structural Analysis

Microstructural characterization was performed with a digital light microscope VHX600 (Keyence, Neu-Sienburg, Germany) and a scanning electron microscope Nova NanoSEM 450 (FEI, Hillsboro, OR, USA).

Cross-sections were prepared from the samples by embedding and stepwise grinding and polishing with diamond suspension from 15 µm to 0.25 µm.

The micro-computed X-ray tomography (µCT) scans were performed with a Zeiss Xradia versa (Zeiss, Oberkochen, Germany) using 100–140 kV and 7–10 W depending on the metal content, resulting transmission and detector intensity. For high resolution, the magnification was chosen to be 20x with high emission filters. The voxel size was between 650 and 750 nm for each axis. The scans were analyzed and simulated with the software VGStudioMax (version 3.4.3) by Volume Graphics (Heidelberg, Germany).

2.5. Mechanical Properties

The Young's modulus was measured according to the impulse excitation technique by a Grindo sonic MK5 (GrindoSonic, Heverlee, Belgium) and was calculated with respect to DIN EN 843-2 [16]. The samples were prepared using a 40 mm die by heating up with 50 K/min to 1600 °C and a dwell time of 5 min. The heating rate has been decreased in comparison to the samples for the functional characterization due to limited power capacity by the SPS.

3. Results

3.1. Raw Materials

Table 1 presents representative values for the single deciles. Martoxid demonstrates a median particle size of almost one order of magnitude lower than CT9FG, while Alodur exhibits the highest values with a d_{50}-value of approximately 96 µm. Martoxid exhibits a nearly spherical particle morphology, while fine alumina CT9FG appears more rounded and flake-like. The particle size distributions indicate a very sharp peak around the median for Alodur with a small fine-grained content in the nanometer range. The finer powders also exhibit peaks but over a broader particle size range (Figure 2). While the fine powders Martoxid and CT9FG show a tendency for agglomeration, Alodur appears to be remarkably flowable with a glass-like morphology and sharp-edged particles (Figure 3).

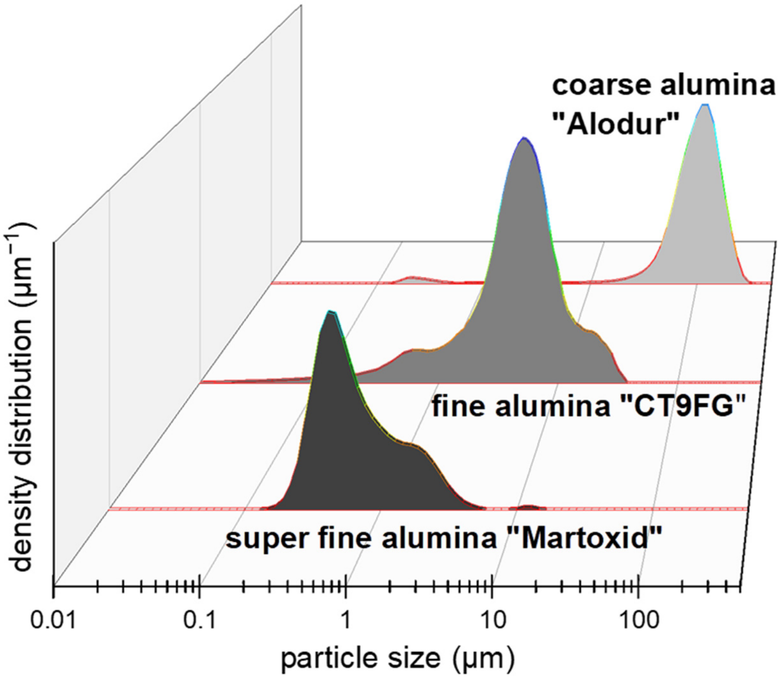

Figure 2. Particle size distribution of the different alumina powders.

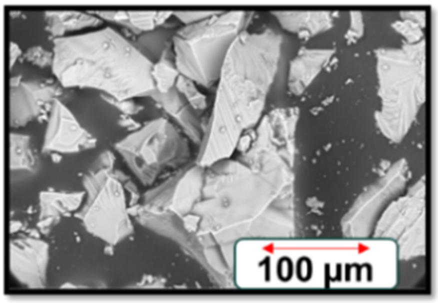

(**a**)

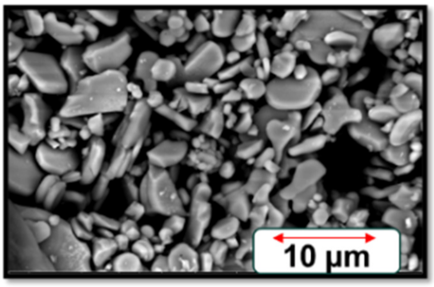

(**b**)

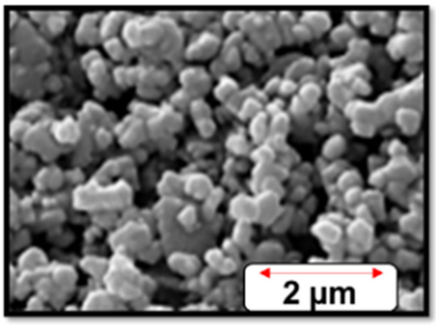

(**c**)

Figure 3. Microscope images of the alumina powders (**a**) Alodur (coarse), (**b**) CT9FG (fine) and (**c**) Martoxid (superfine, source: martoxid powder, Huber advanced).

Table 1. Particle size distribution of different used raw materials.

Raw Material	d_{10} (µm)	d_{50} (µm)	d_{90} (µm)
niobium	8.17	34.2	70.68
tantalum	6.07	32.18	68.0
coarse alumina "Alodur"	44.83	95.78	162.35
fine alumina "CT9FG"	0.98	4.7	12.14
superfine alumina "Martoxid"	0.15	0.71	2.51

The metal powders show similar decile values and are therefore largely comparable in the particle size distribution. The difference is primarily in the small fine content of the tantalum powder (see Table 1).

3.2. Comparison of SPS with Conventional Sintering

The comparison in Figure 4 of a conventional sintering process with preshaping by uniaxial pressing with and without cold isostatic pressing shows a significant difference in densification compared to SPS (here for Nb/Al_2O_3 20/80 (coarse/superfine alumina 50/50). The powder mixtures are very sensitive to CIP (400 MPa, 90 s), which can lead to cracks after pressing. These results highlight the advantage of SPS for obtaining dense metal–ceramic composites [17].

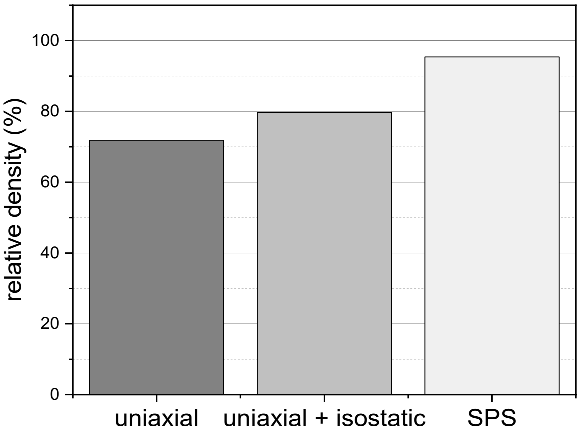

Figure 4. Comparison of relative densities after sintering at 1600 °C by conventional route (dwell time 2 h) and SPS for Nb/Al_2O_3 20/80 (coarse-grained/superfine-grained alumina 50/50).

In particular, the coarse alumina matrix is difficult to densify by conventional sintering without pressure. In this context, SPS combines pressure-assisted compaction and rapid Joule-heating-assisted sintering, resulting in significantly improved densification. It must be kept in mind that sintering temperatures can be limited by the reaction of aluminum oxide and carbon at ~1800 °C [18,19].

3.3. Densification and Electrical Properties

3.3.1. Metal-Alumina Composites with Different Compositions

The densification diagrams for the metal-alumina compositions in Figure 5 (metal/fine alumina and metal/coarse alumina) show a clear dependency on sintering temperatures, alumina matrix and metal contents. While the composition with the coarse-grained alumina has lower densities for every sintering temperature, the values for the fine-grained CT9FG are >97% for T_{sinter} = 1600 °C, which align well with the results of Kraft et al. [20]. The results indicate that densification of the fine-grained CT9FG matrix increases markedly between 1400 and 1500 °C. While sintering at 1400 °C, relative densities are below 80%, whereas increasing the temperature to 1500 °C leads to an increase to more than 90% relative density.

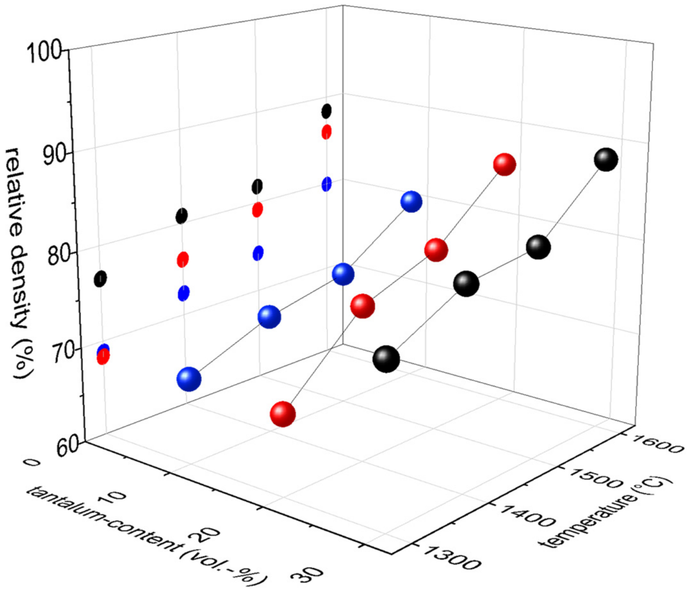

(**a**)

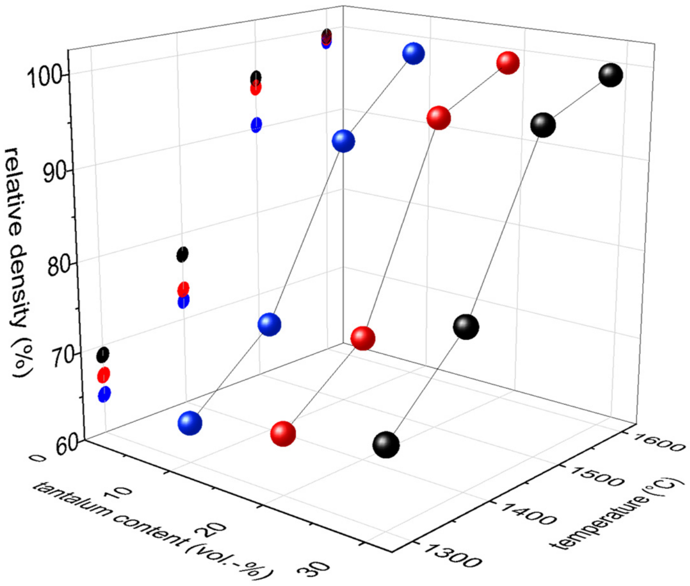

(**b**)

Figure 5. 3D densification maps for Ta/coarse alumina (**a**) and Ta/fine alumina (**b**) with metal contents from 10 to 30 vol.%.

Figure 6 shows the different specific conductivities depending on metal content and measured direction, referring to anisotropic electrical properties, later explained by microstructure and texture. The conductivity measured parallel to the applied pressure is lower than that measured perpendicular to the pressure direction. The coarse-grained composition has higher anisotropy than the fine-grained; independent of the metal content, the difference stays almost uniform. The observed anisotropic conductivity indicates direction-dependent metal-phase connectivity; its possible relation to SPS current paths and microstructural evolution is discussed in Section 4. Comparable orientation-dependent electrical responses have recently been reported for SPS-processed ceramic composites containing aligned conductive phases, where the measurement direction relative to the pressing direction strongly affects charge transport through the conductive network [21].

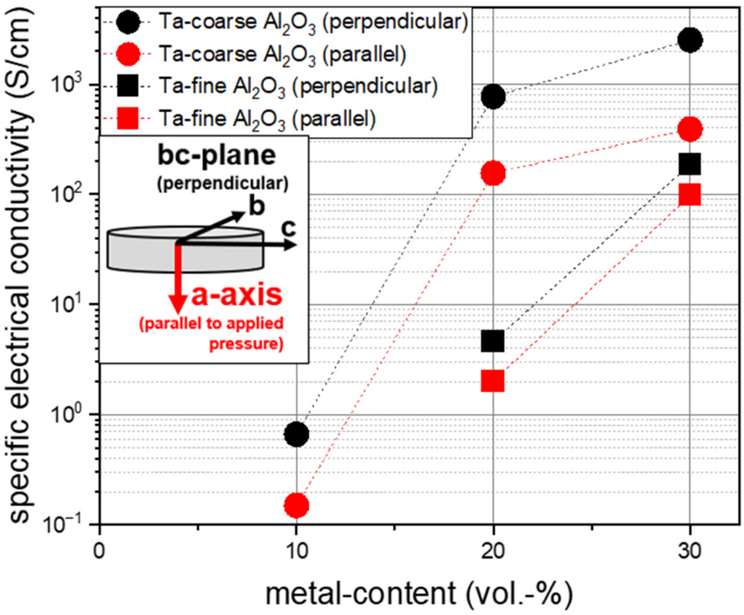

Figure 6. Anisotropic conductivity for compositions with different metal contents and alumina powder for sintering temperature at 1600 °C.

The composites showed partially carbide phases after sintering, most likely due to a reaction at elevated temperatures with the graphite tool [22]. Further investigations are planned to analyze the influence of carbon diffusion. An overview of SPS phenomena is given in [17,23].

As a verification, the pure refractory metals niobium and tantalum could be densified with the standard parameters (1600 °C, 50 MPa, 5 min dwell time) to more than 95% relative density, while the measured electrical conductivity aligned well with the literature values [24].

3.3.2. Metal-Alumina Composites with a New Matrix Composition

Combining different alumina powders makes it possible to exploit both key effects: deformation and densification. The matrix composition was adapted with a mixture of coarse- and fine-grained alumina in different vol.-ratios. Figure 7a shows the different particle size distributions for the modified alumina matrices, which align well with the expected mixture ratios of both powders. While the coarse/fine compositions lead to distributions with three significant peaks (trimodal), the coarse/superfine composition shows the two major peaks of every single distribution also in the combined mixture (bimodal).

Figures 7b and 8 show the significant effect of the superfine-grained alumina powder with a d_{50} size approximately one order of magnitude smaller. While the effect for the ratios coarse/fine 75/25 coarse/superfine 75/25 is almost negligible, the 50/50 compositions evidently demonstrate the initiation of the sintering process at lower temperatures, accompanied by better densification with superfine alumina. At T_{sinter} = 1300 °C the difference ranges between 5 and 10 points when comparing coarse/fine (Alodur/CT9FG) and coarse/superfine (Alodur/Martoxid) matrix compositions. All the compositions show the same trend that a higher metal content leads to better densification. The differences vary but reach up to 5 points when comparing metal contents of 10 and 30 vol.-%.

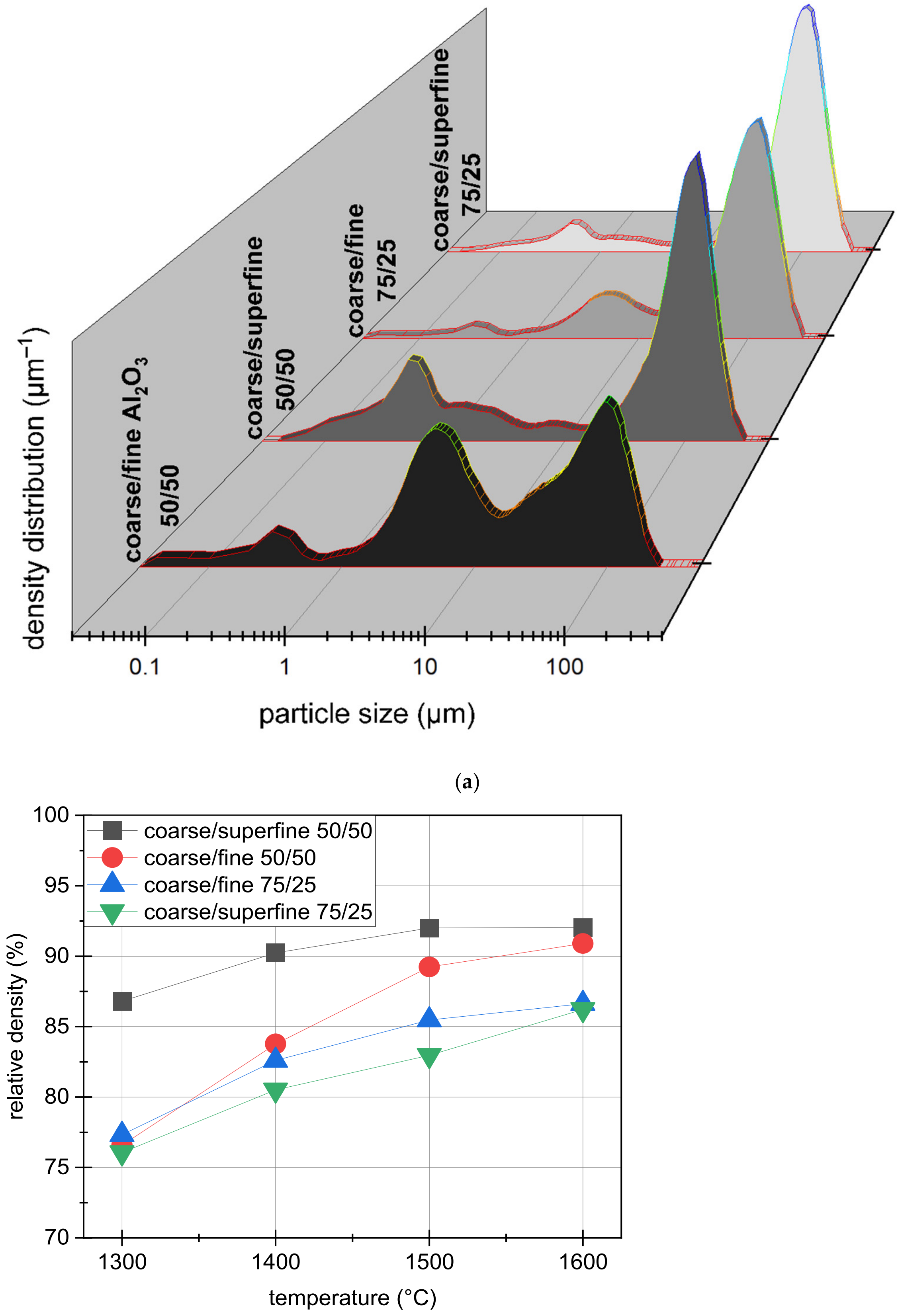

(**a**)

(**b**)

Figure 7. Particle size distributions of different matrix alumina mixtures (**a**) and their densification behavior via SPS (1600 °C, 5 min) (**b**).

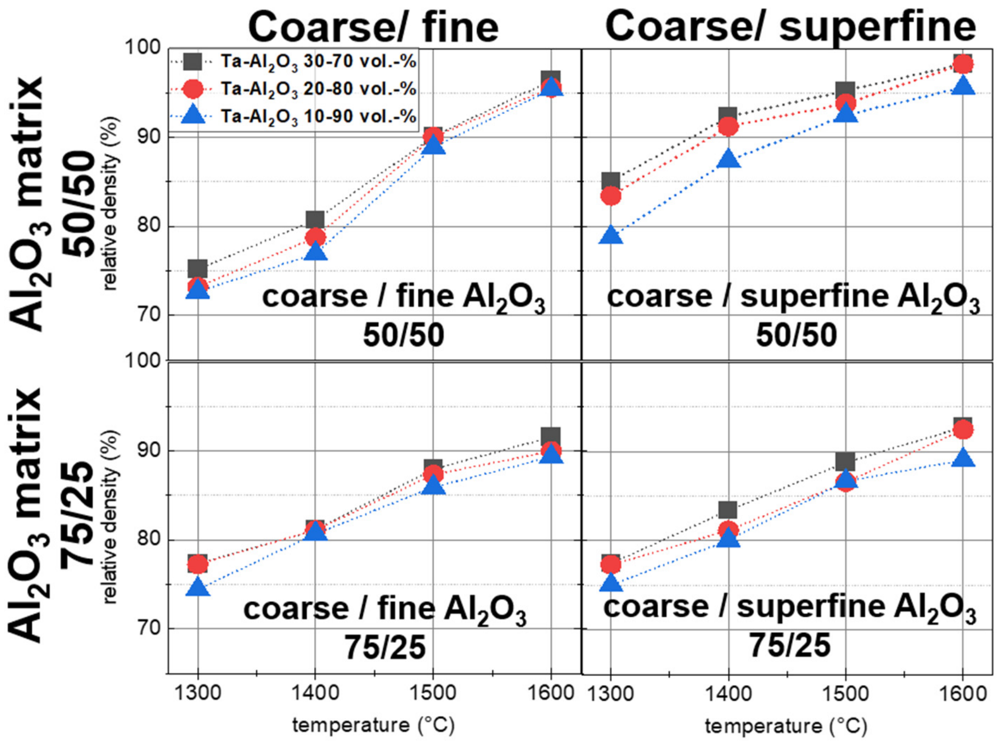

Figure 8. Densification map for Ta/Al_2O_3 (coarse/fine and coarse/superfine in ratios of 50/50 and 75/25 vol.-%).

Comparing the resulting electrical conductivities in Figure 9, a clear difference can be observed depending on the matrix composition not only in the conductivity values themselves but also in the percolating or non-percolating behavior and therefore non-measurable state. With a finer matrix grade, a decreasing conductivity for the same metal content and, above all, a smaller likelihood of percolation is observed.

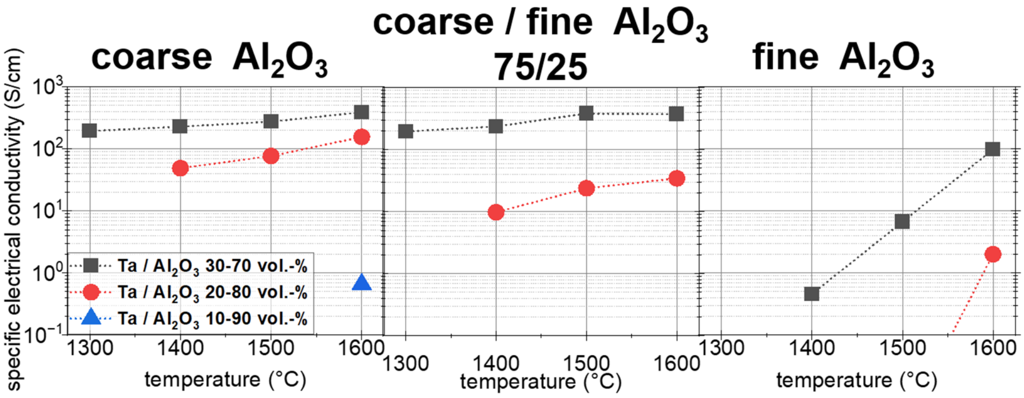

Figure 9. Electrical conductivity of Ta/alumina composites, depending on sintering temperatures and matrix compositions.

Compositions with 30 vol.-% metal content and a coarse-dominated matrix show similar conductivities independent of sintering temperature. Two conclusions can be drawn from this result. By adjusting porosity through lowering sintering temperatures, similar electrical properties can be achieved at lower sintering temperatures, which may be relevant for reducing energy consumption. With an increased fine content up to 25 vol.% in the alumina matrix, it seems to be the case that the matrix here does not affect the metal paths for 30 vol.-% metal content, although densification is improved (see Figures 5a and 8). A decrease in the amount of metal present is accompanied by a reduction in the intensity of the effect. This behavior cannot be clearly transferred to fully fine-grained matrices. (Figure 9, right). These results resemble each other for the compositions with tantalum or niobium.

3.4. Microstructural Characterization

Figure 10 shows the comparison of the microstructure between a coarse-alumina and a fine-grained alumina matrix (gray), each of them with 20 vol.-% metal content. The deformation of the metal phase (white) is more elongated for the coarse-grained composition (Figure 10a). The finer matrix seems to provide better embedding with fewer contact points between the single particles and shows a very dense microstructure with almost no porosity (Figure 10b).

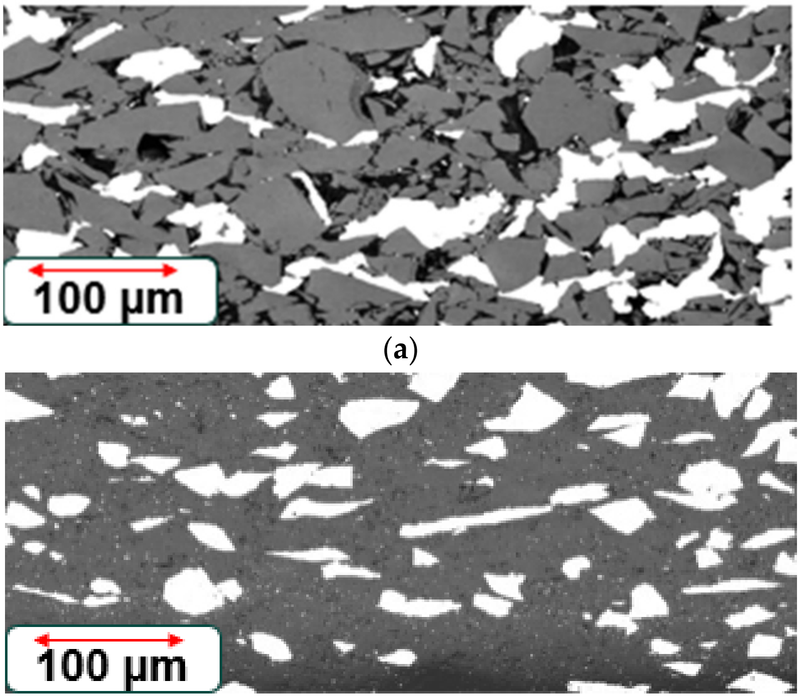

Figure 10. Comparison between the microstructure of Ta/coarse alumina 20/80 (**a**) and Ta/fine alumina 20/80 (**b**) vol.-%.

Figure 11 shows the microstructural evolution of a niobium/alumina composition with increasing metal content from 10 to 30 vol.-%, while the alumina matrix consists of 50/50 vol.-% of coarse-grained Alodur and superfine-grained Martoxid. The micrographs show the evolution of the metal network with increasing metal content. For the 30 vol.-% composition, a connected metal network is already apparent in the 2D micrograph.

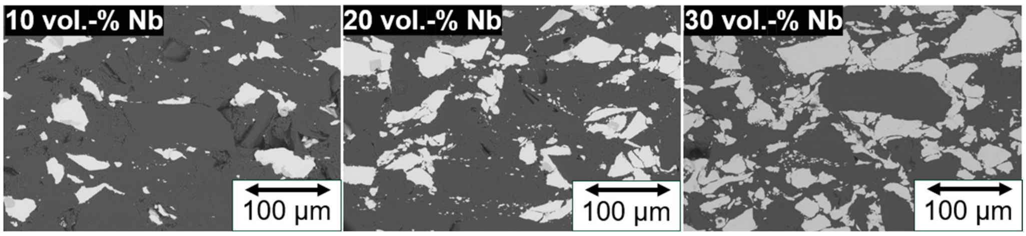

Figure 11. Microstructural development of Nb/Al_2O_3 (coarse/superfine 50/50) with increased metal content.

3.5. 2D-Circularity Analysis of the Metal Particles

To support these visual and experimental investigations, the deformation behavior of the metal particles was evaluated as a function of the surrounding matrix (Figure 12). Particles with a diameter smaller than 10 µm were not included due to the limited deformation and therefore deviating influence. These particles are mostly located in the pores and were not affected by the deformation mechanism.

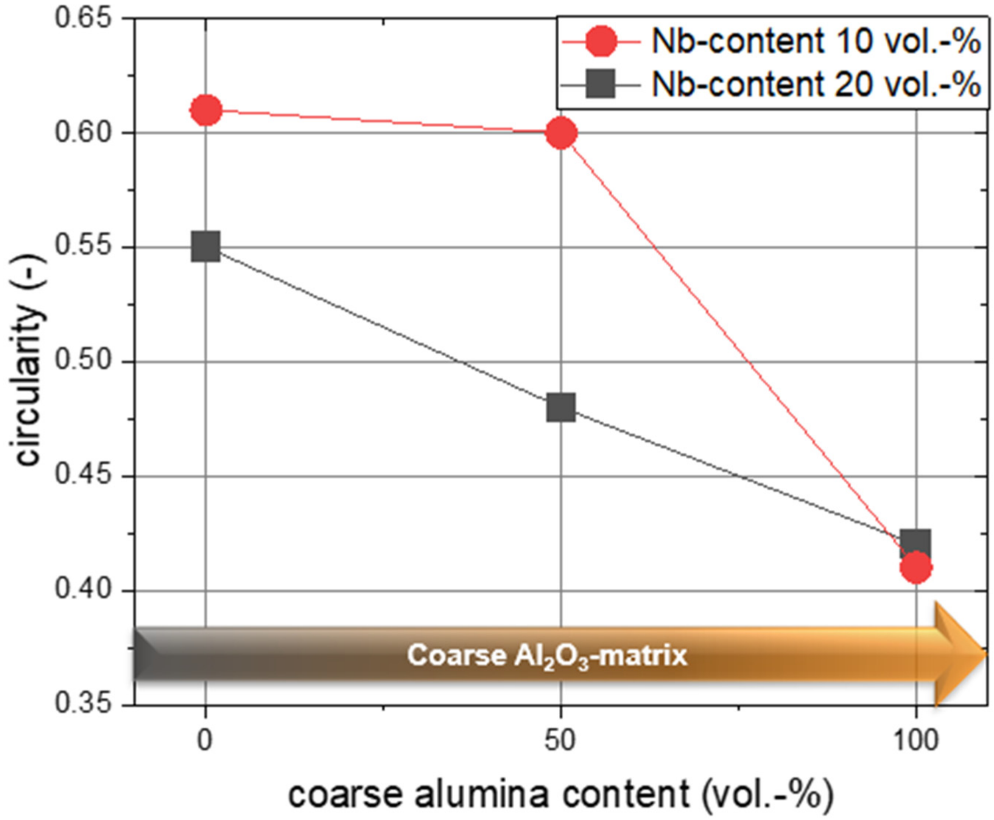

Figure 12. Circularity analysis of elongated metal particles after sintering depending on the alumina matrix composition.

The analysis for different metal content quantitatively shows the deformation in a coarse-grained matrix, which leads to lower circularity values of around 0.42 compared with an average value of approximately 0.61 for the fine-grained matrix.

The 2D circularity of the metal particles in polished cross-sections was calculated using

$$circularity = \frac{4 \cdot \pi \cdot area}{perimeter^2} \quad (3)$$

Figure 13 shows the comparison in specific electrical conductivity between the µCT-based simulation and experimental results, which agree well with each other, with a slightly higher simulated value than determined experimentally. This can be explained by the transfer losses of applied electrodes, compared with the assumed ideal electrode in the simulation software.

Thus, due to the high density and atomic mass of the refractory metals, the quality of scans with respect to intensity and transmission is reduced or requires substantially longer acquisition times with increased metal content. Therefore, only smaller areas with voxel sizes of around 600–700 nm were scanned over the whole range up to 30 vol.-% with acceptable resolution. The observation that a small, randomly selected area exhibits results that are nearly identical to those of the macroscopic sample indicates a relatively homogeneous distribution of the metal phase within the investigated volume. Figure 13a also shows that metal content closer to the percolation threshold leads to larger differences in results because the statistical probability for the same properties microscopically and macroscopically decreases.

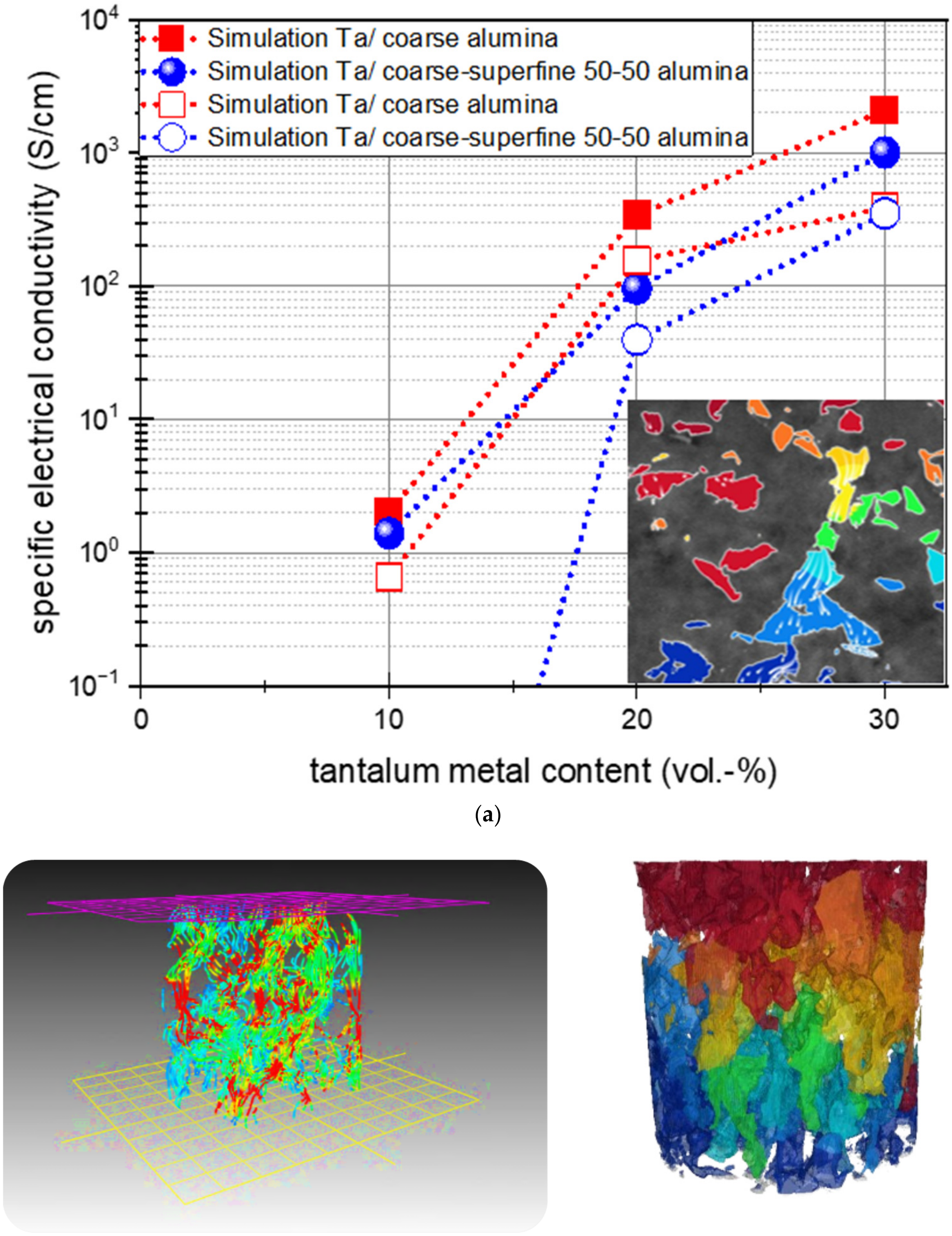

(**a**)

(**b**) (**c**)

Figure 13. Comparison between µCT-based simulation and experimental results of Ta/alumina (coarse/superfine 50/50) composites (**a**), µCT analysis with visualization of conducting paths (**b**) and simulated body (**c**).

3.6. Percolation Theory

From the perspective of percolation theory, minimizing the metal content required to form a conductive network is essential for reducing material costs [20,25]. Recent continuum-percolation models for anisotropic particles show that excluded area, particle orientation and average connectivity at the threshold must be considered when interpreting conductive network formation [26]. This is particularly relevant for the present composites, where SPS-induced deformation of the metallic phase leads to elongated and direction-dependent conductive pathways. Figure 14 should be read in a way that for a given composition and sintering temperature, a certain metal content is required for the sample to become measurably conductive. With respect to that, an operational percolation threshold of 7.5 vol.-% was obtained under the applied measurement criterion, indicating highly effective metal-phase connectivity after SPS, which is consistent with the results reported by Kraft et al. [14]. The threshold was checked stepwise by decreasing the metal content for 2.5 percentage points. Berkowitz mentioned in [27] that the percolation threshold, for a three-dimensional, two-phase composition, is p_{crit} = 24.9 vol.-% for a conventional simple-cubic lattice in a bond percolation model, while 31% for a site-bonded model, which can be seen here as a landmark for common percolation models, although this composite system consists of randomly packed particles, which requires new approaches [28,29].

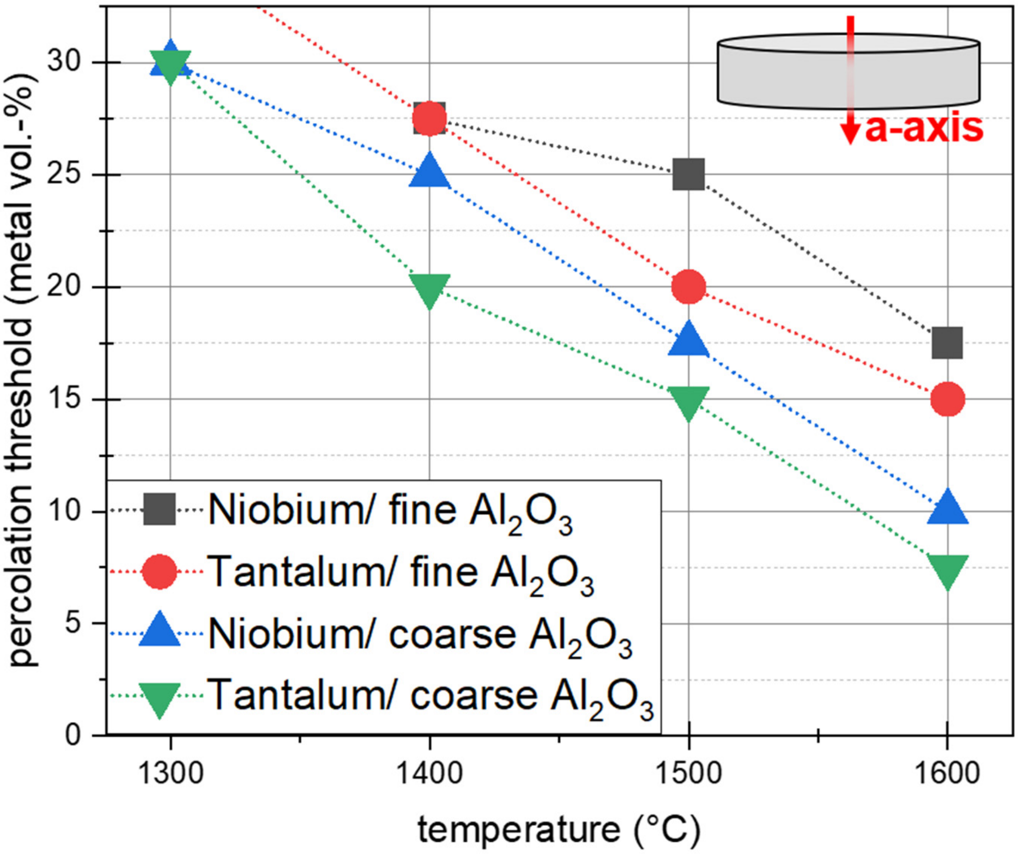

Figure 14. Sintering temperature dependent percolation threshold for Ta/Nb-Alodur/CT9FG compositions.

Additionally, it must be kept in mind that the investigated system does not only consist of two phases (ceramic and metal), but of three since porosity represents an additional non-conductive phase that may interrupt conductive pathways. This further underlines the significance of the low operational percolation threshold.

An adapted matrix composition leads to a reduction in the percolation threshold, particularly at low temperatures (Figure 15). Here the percolation threshold can be reduced by up to 50%, which could contribute to a significant reduction in material costs.

https://doi.org/10.3390/met16070742

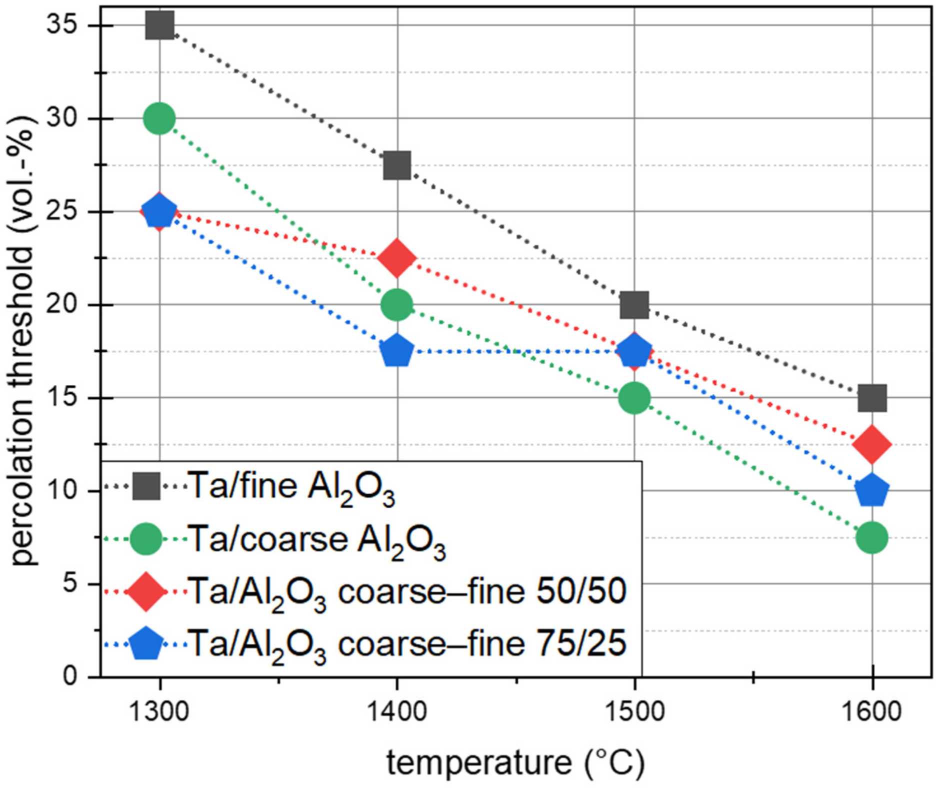

(**a**)

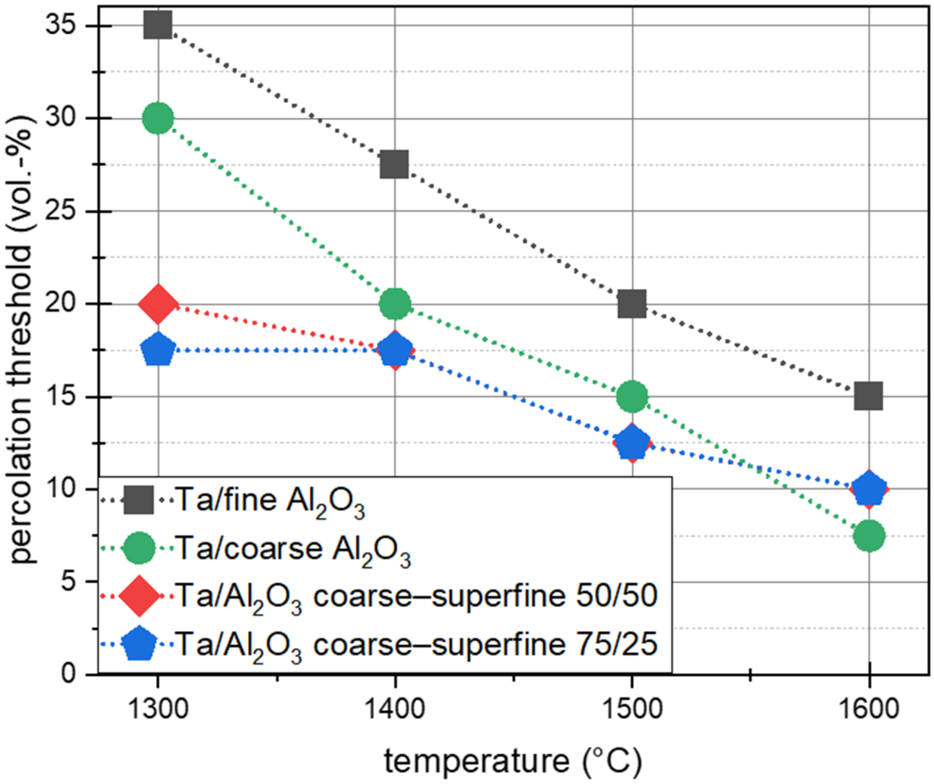

(**b**)

Figure 15. Effect of matrix mixtures on percolation threshold on the Ta/alumina system for Ta/coarse-fine alumina (**a**) and Ta/coarse-superfine alumina (**b**).

3.7. Mechanical Properties

In Figure 16, both compositions show higher stiffness for the niobium variant. But with rising metal content, the trends are inverse to each other. While fine-grained alumina decreases in E-modulus, the coarse-grained matrix leads to higher values, which may increasingly reflect the contribution of the metallic phase with rising metal content. The literature and suppliers could not provide an E-modulus for the Alodur bulk material. It must be mentioned that even with the standard SPS parameters, Alodur reaches relative densities of only 75–80%. As an assumption, the E-modulus of Alodur was calculated based on the model by Spriggs [30]. The number of tested samples is between 25 and 35.

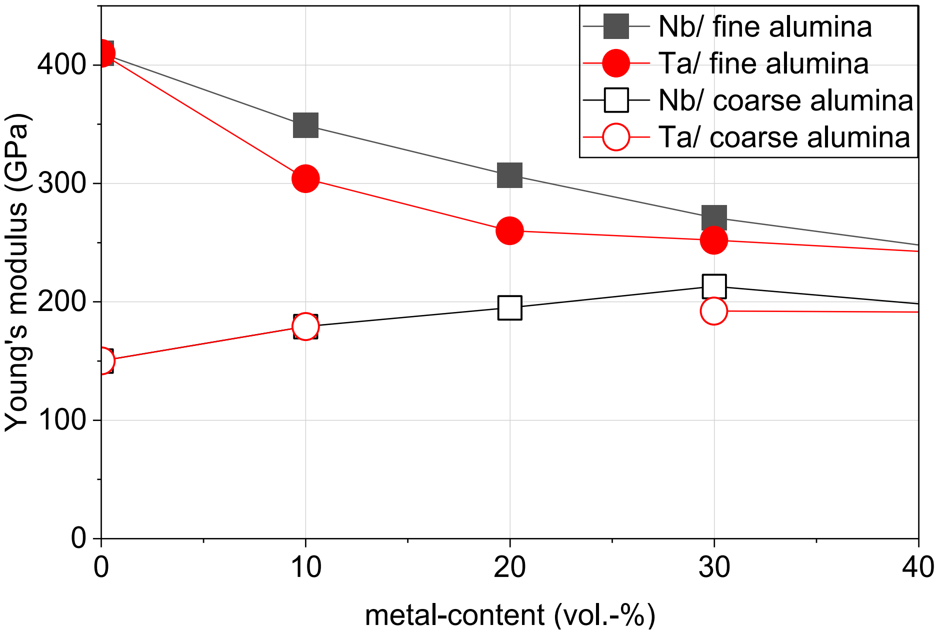

Figure 16. E-Modulus for Nb/Ta–coarse-grained/fine-grained alumina compositions with metal contents from 10 to 30 vol.-% and sintered with SPS standard parameters (1600 °C, 5 min).

Dotta et al. [31] confirm the decreasing influence of a higher metal content on the E-modulus, which aligns with our results for the fine-grained CT9FG.

Deeper insights regarding mechanical properties, especially for high temperature, are shown in [32,33].

4. Discussion

The results demonstrate the importance of the chosen processing route for densification and functional property development. Compared with the conventional route, cold isostatic pressing increases the relative density by almost 10 percentage points; however, the powder mixtures appear to be highly pressure-sensitive, probably due to the elastic response of the metallic phase, which may lead to crack formation after pressing [34,35]. In contrast, SPS enables substantially higher densification by combining uniaxial pressure, rapid heating and short dwell times.

Regarding the effect of spark plasma sintering parameters, two clear tendencies can be observed. Higher metal content leads to a better filling of the porosity by the metal, additionally supported by an increased plastic behavior of the metal with higher sintering temperatures. Secondly, higher temperatures lead, as expected, to better densification.

The different kinds of raw alumina lead to two key effects while sintering. The coarse alumina enhances the deformation of the plastic deformable metal phase and increases the aspect ratio of the metal particles. Considering the particle morphology shown in Figure 3, the sharp edges of the coarse alumina particles may promote localized deformation of the metallic phase. Due to the coarse microstructure, which can only be densified to a limited extent, the metal phase can elongate into the pores, particularly perpendicular to the applied pressure. That leads to an anisotropic microstructure, resulting in direction-dependent electrical conductivities (Figure 6) and texture (Figure 10). Fine-grained alumina has been demonstrated to enhance the sintering process, leading to improved and earlier densification, explained by the well-known size-dependent sintering behavior of smaller particles [5,36,37]. Additionally, the application of balanced forces is promoted, reducing metal elongation. The alumina particles do not show any significant change in morphology. The results of Weiner et al. further support the relevance of particle morphology for sintering activity [38,39].

The mentioned sintering characteristics provide a wider variety of composite properties to include the effects of coarse-grained and fine-grained alumina. The key aspect for a modified alumina matrix is the combination of both mechanisms working as a trade-off between better densification and higher deformation of the softer phase (here metal). The difference between the alumina ratios can be explained by the ideal packing of the alumina mixtures [40]. While a fine content of 25 vol.-% is not sufficient to fill the porosity of a coarse matrix, it still improves densification, while a percolating network formation benefits from the higher aspect ratios. Martoxid seems to densify superiorly compared to the fine CT9FG, leading to higher values of conductivity and demanding lower sintering temperatures for percolation.

The investigation of the percolation threshold in Figure 15 showed that both effects add to each other. The results indicate that an adapted alumina matrix contributes to a percolating structure for lower temperatures. This suggests an ideal ratio between densification for lowering distances between particles and enough room for elongation of the conductive phase. This raises the question of whether there is a critical correlation between densification and metal content, combined with the results of aspect ratios/circularity and size of the metal particles. Further investigations will examine this correlation, supported by 3D-analysis with µCT to include geometrical aspects like tortuosity in these considerations.

The results of the electrical properties provide insights into how different compositions densify, depending on current flows only through the tools or also through the powder/sample. The densification map in Figure 5, combined with the results relating to percolating or isolating electrical properties, explains when the current flow approximately changes during the process. The spark plasma sintering process depends not only on metal content and sintering temperature but also on the time required to form an electrically conductive network within the compact, i.e., a sintered body, which modifies the current flow during sintering. Initially, during the heating process, the current is predicted to flow exclusively through the graphite tools. The beginning is controlled by indirect heating induced by the graphite. The sample is primarily heated by conduction; as the temperature rises, the amount of thermal radiation increases [5]. In regard to the relatively high thermal conductivity of alumina [41] for a ceramic material, in addition to the metal phase, a homogeneous heat transfer is expected while sintering.

However, concurrently, an enhancement in the densification and plastic deformation of the metal phase occurs. Consequently, developing percolating networks may carry part of the current. This affects the sintering mechanisms and the phenomena occurring during SPS [42,43]. High current densities at the first necks in the network are expected and would therefore lead to high temperatures [3]. Further formation of the network should engender a more homogeneous current flow and temperature distribution. This may also contribute to particle-surface cleaning, as discussed in SPS literature [44]. Additionally, thermal gradients are reduced by better volumetric thermal conductivity [45]. This higher conductivity should now be considered with respect to the temperature-dependent conductivity of graphite to assess the preferred pathway for the current and therefore also the resulting heating mechanism in the green body.

It seems that there is no clear dependency between densification, percolation and electrical conductivity. This suggests a multifactor dynamic relationship which is characterized by reciprocal influence and interaction between the input parameters and resulting properties (see Figures 5, 8 and 9).

The assertion that elevated densification results in enhanced conductivity is only applicable to each specific composition. In this instance, higher densification is observed due to higher sintering temperatures, accompanied by enhanced conductivity. It is imperative to consider the potential of a matrix to densify prematurely, as this phenomenon could impede the percolation of a network by obstructing potential pathways.

Regarding the mechanical results, a significant indicator for percolation was not found. It must be kept in mind that percolation is not uniform for different characteristics. Therefore, it can be assumed that the electrical percolation threshold varies from the mechanical threshold. It can be asked here whether mechanical properties show a smoother transformation from non-percolating to percolating composition by developing a network which becomes stronger with better interconnection and thicker paths. While electrical conduction can occur through very small, connected pathways and shows a punctual steep increase from an insulating to a conducting state at the moment a network is created, which would be even the case for a sufficiently small metal path, mechanical properties are expected to increase more steadily.

Microstructural evolution in Figure 11 visualizes the mentioned effects. Due to its larger particle size by a factor of $(\sim 20\times)^3$ (~100 μm vs. 5 μm) compared to CT9FG, a single particle of coarse-grained Alodur results in a reduction in possible paths for metal particles due to their volume. This, in turn, increases the possibility of interconnecting paths by forcing the metal into more concentrated areas. The additional effect of deformation serves to further enhance interconnectivity. These more concentrated areas are now better densified by the presence of superfine or fine-grained alumina.

The slightly higher conductivity of tantalum compared to niobium can be attributed to the enhanced conductivity of tantalum composites [24]. A more salient difference, however, is the lower percolation threshold, which is contingent on the structural condition. This can be determined through an examination of particle size distribution.

Tantalum has a fine particle fraction with particle sizes of 200–500 nm. SEM images (Figure 17a) show that these particles form fine aligned networks around the alumina particles in the outer regions of the sample [46]. The observations may indicate an electromigration-related effect, as discussed for SPS processes in the literature, which remains difficult to verify experimentally [5,17,42]. The high current could exert a directed force on the particle motion. The possibility of other typical SPS phenomena like the Peltier effect, which could influence the temperature and current distribution [5] locally, should also be considered here as an additional factor.

Therefore, the results may indicate that a modified particle size distribution for the metal phase can lead to higher conductivity at the same or even lower metal content as well as a reduction in the percolation threshold [20].

To strengthen that argumentation, the number of particles for a median d_{50} particle with ~30 μm can be compared with that of two orders of magnitude smaller fine particles. Regarding the volume, one large particle is equivalent to 10^6 smaller particles with a length of 30 cm if they were perfectly aligned, demonstrating the potential effect on structural conditions. Experiments showed that the conductivity could be increased at the same metal content of 10 vol.-% by almost two magnitudes for the Ta (fine particles)/coarse alumina composition. In general, it can be stated that smaller particles influence the percolation threshold by decreasing the statistical distance between each other and enhancing the formation of a network [46]. Some publications even regard electron tunneling as a possible factor, where electrons could pass even due to thin, insulating contact points [47,48], which may also contribute to the observed electrical behavior.

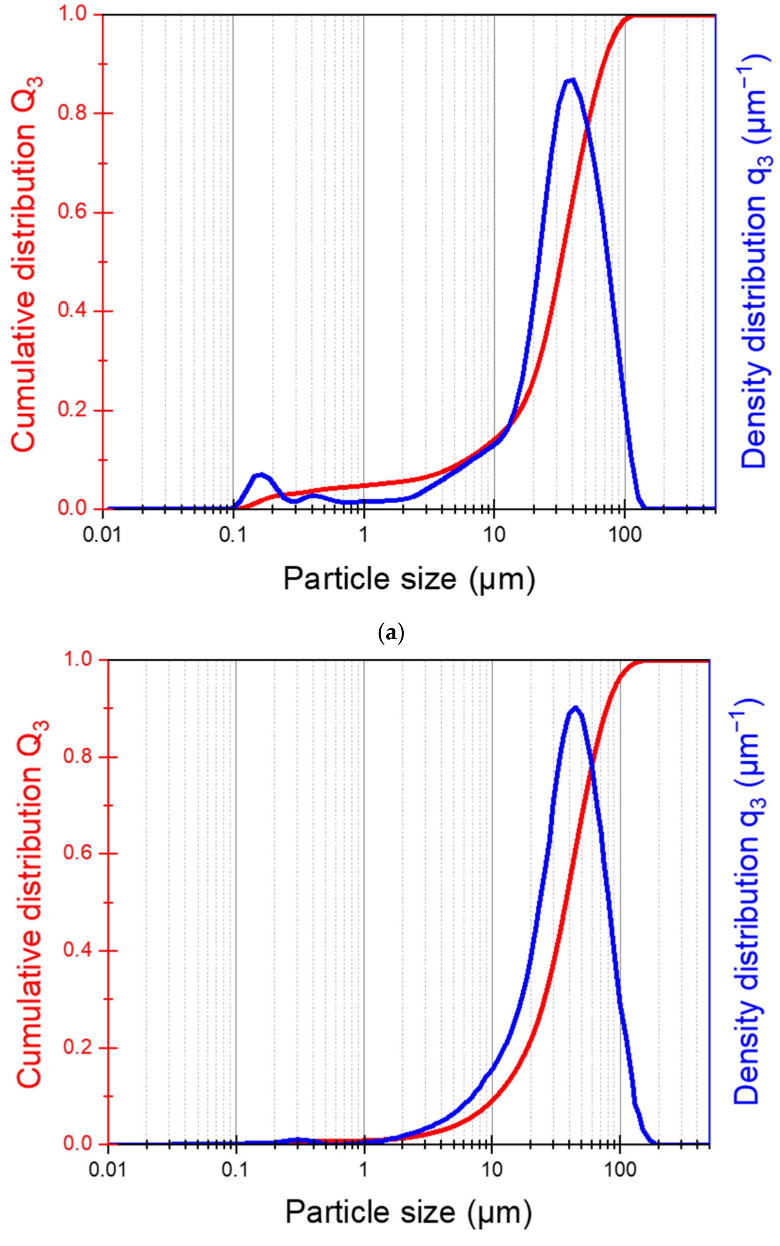

(**a**)

(**b**)

Figure 17. Particle size distribution of the raw materials tantalum (**a**) and niobium (**b**).

To investigate whether current-path-dependent particle migration may contribute, a Ta/Alodur 10/90 sample was sintered with electrically isolating alumina disks at the upper and lower punch. Migration is not detectable anymore at the top and bottom of the sample but is only observed at the right and left sides of the disk-shaped sample, where the specimen still has physical contact with the conducting graphite foil. Also, the grayish area (Figure 18b), which showed a macroscopic core–shell structure before, seems ring-shaped with the insulation setup.

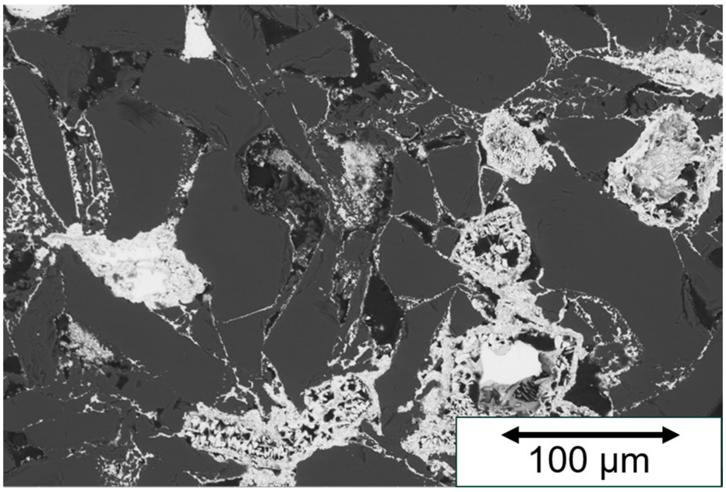

(**a**)

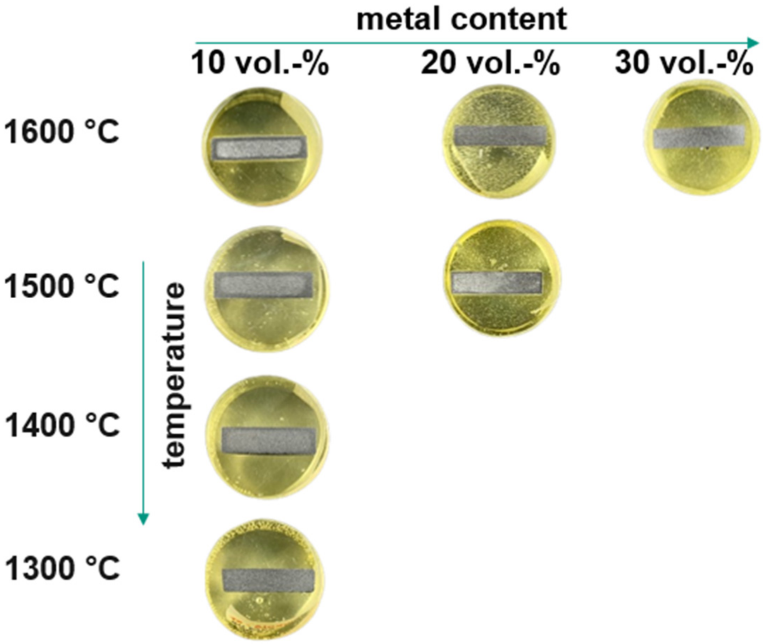

(**b**)

Figure 18. Networks of nm-sized tantalum particles for Ta/coarse/alumina 10/90 in the outer area of the sample (**a**), Visual difference in embedded specimen of Ta/coarse alumina 10/90 depending on metal content and sintering temperature (**b**).

The different grayish coloration is consistent with possible carbon diffusion and/or carbide formation, but further phase analysis is required.

The carbide phases are not assumed to influence the functional properties and percolation significantly. Otherwise, the compared results of µCT-based analysis and experiments (Figure 13a), especially for electrical conductivity, would have shown a substantially higher deviation.

5. Conclusions

This study demonstrates that the alumina matrix composition strongly affects densification, metal-phase deformation and electrical percolation in SPS-processed Ta/Nb-Al_2O_3 composites. The results show that matrix-controlled deformation and spatial distribution of the metal phase govern the formation of conductive pathways.

By adjusting the composition, densification can be varied from approximately 70% to almost 100%, while the electrical conductivity can be tuned over ten orders of magnitude for metal contents of up to 30 vol.-%. The results demonstrate that percolation can occur with metal contents of only 7.5 vol.-%. Further investigation indicates that this could be even further improved by varying the metal particle size distribution, including a higher content of very fine particles.

Tailored mixtures of coarse and fine or superfine alumina provide a promising route to combine the effects of deformation and densification. In conclusion, this allows the reduction in the required refractory metal content while maintaining electrical functionality and sintering at lower temperatures for a less energy-consumptive process.

Microstructural results confirm these findings by showing a pressure direction-dependent elongation of metal particles and analyzing circularity. The coarse-grained alumina composition shows higher aspect ratios of the metal than the fine-grained alumina composition and, in conclusion, lower circularity of 0.42 compared to 0.61 for a fine-grained composition. µCT-based simulation confirms our results with analysis of the properties and structure. Simulated conductivities match well with the experimental findings, supporting the assumption about the structural influence of metal and alumina.

These findings can be broadened in further work by an interconnected model of electrical, mechanical and structural properties. A deeper understanding could be gained by applying different models (e.g., effective medium theory).

Author Contributions: Conceptualization, G.K., S.W. and K.G.S.; methodology, G.K., S.W. and K.G.S.; formal analysis, G.K.; investigation, G.K., S.W. and K.G.S.; writing—original draft preparation, G.K.; writing—review and editing, S.W. and K.G.S.; visualization, G.K.; software, validation, resources, data curation, supervision, project administration, funding acquisition. All authors have read and agreed to the published version of the manuscript.

Funding: This research was funded by the German Research Foundation (DFG) within Research Unit FOR 3010 (project number 416817512).

Data Availability Statement: The data that support the findings of this study are available from the corresponding author upon reasonable request.

Acknowledgments: The authors thank Noel Noller for technical assistance with sample preparation and measurements.

Conflicts of Interest: The authors declare no conflicts of interest.

References

1. Ruela, V.; van Beurden, P.; Luchini, B.; Hofmann, R.; Birkelbach, F. Optimizing the Steel Ladle Thermal Management: Toward a Sustainable and Cost-Effective Ladle Fleet Logistics. *Steel Res. Int.* **2024**, *96*, 2400616. [CrossRef]
2. Yang, L.; Peng, P.; Weger, N.; Mills, S.; Messeri, C.; Menon, A.K.; Zeltmann, S.; Babbe, F.; Zheng, Q.; Dun, C.; et al. Self-Heating Conductive Ceramic Composites for High Temperature Thermal Energy Storage. *ACS Energy Lett.* **2025**, *10*, 1002–1012. [CrossRef]
3. Bubesh Kumar, D.; Selva babu, B.; Aravind Jerrin, K.M.; Joseph, N.; Jiss, A. Review of Spark Plasma Sintering Process. *IOP Conf. Ser. Mater. Sci. Eng.* **2020**, *993*, 012004. [CrossRef]
4. Chen, W.; Anselmi-Tamburini, U.; Garay, J.E.; Groza, J.R.; Munir, Z.A. Fundamental investigations on the spark plasma sintering/synthesis process. *Mater. Sci. Eng. A* **2005**, *394*, 132–138. [CrossRef]
5. Guillon, O.; Gonzalez-Julian, J.; Dargatz, B.; Kessel, T.; Schierning, G.; Räthel, J.; Herrmann, M. Field-Assisted Sintering Technology/Spark Plasma Sintering: Mechanisms, Materials, and Technology Developments. *Adv. Eng. Mater.* **2014**, *16*, 830–849. [CrossRef]
6. McLachlan, D.S.; Blaszkiewicz, M.; Newnham, R.E. Electrical Resistivity of Composites. *J. Am. Ceram. Soc.* **2005**, *73*, 2187–2203. [CrossRef]
7. Ambrožič, M.; Lazar, A.; Kocjan, A. Percolation threshold in ceramic composites with isotropic conducting nanoparticles. *J. Eur. Ceram. Soc.* **2020**, *40*, 1684–1691. [CrossRef]

8. Kraft, B.; Wagner, S.; Schell, K.G.; Hoffmann, M.J. Field-Assisted Sintering of Nb–Al_2O_3 Composite Materials and Investigation of Electrical Conductivity. *Adv. Eng. Mater.* **2022**, *24*, 2200063. [CrossRef]
9. Peretyagin, P.; Yanushevich, O.; Krikheli, N.; Pristinskiy, Y.; Solis Pinargote, N.W.; Smirnov, A.; Grigoriev, N. Production and Mechanical Performance of Tantalum Strengthened Alumina–Zirconia Composites with Graphene Addition. *J. Compos. Sci.* **2025**, *9*, 577. [CrossRef]
10. Zienert, T.; Endler, D.; Hubálková, J.; Gehre, P.; Eusterholz, M.; Boll, T.; Heilmaier, M.; Günay, G.; Weidner, A.; Biermann, H.; et al. Coarse-Grained Refractory Composite Castables Based on Alumina and Niobium. *Adv. Eng. Mater.* **2022**, *24*, 2200296. [CrossRef]
11. Günay, G.; Zienert, T.; Endler, D.; Aneziris, C.G.; Biermann, H.; Weidner, A. Influence of particle size and fabrication method on mechanical properties of Nb-Al_2O_3 refractory composites under compressive loads at high temperatures. *Ceram. Int.* **2025**, *51*, 9619–9629. [CrossRef]
12. Gebauer, J.; Franke, P.; Seifert, H.J. Thermodynamic Evaluation of the system Ta–O and Preliminary Assessment of the Systems Al–Nb–O and Al–Ta–O. *Adv. Eng. Mater.* **2022**, *24*, 2200162. [CrossRef]
13. Griffin, A.; Robertson, M.; Gunter, Z.; Coronado, A.; Xiang, Y.; Qiang, Z. Design and Application of Joule Heating Processes for Decarbonized Chemical and Advanced Material Synthesis. *Ind. Eng. Chem. Res.* **2024**, *63*, 19398–19417. [CrossRef] [PubMed]
14. Kraft, B.; Wagner, S.; Schell, K.G.; Hoffmann, M.J. Field assisted sintering of Ta–Al_2O_3 composite materials and investigation of electrical conductivity. *Open Ceram.* **2023**, *13*, 100319. [CrossRef]
15. Zienert, T.; Endler, D.; Hubálková, J.; Günay, G.; Weidner, A.; Biermann, H.; Kraft, B.; Wagner, S.; Aneziris, C.G. Synthesis of Niobium-Alumina Composite Aggregates and Their Application in Coarse-Grained Refractory Ceramic-Metal Castables. *Materials* **2021**, *14*, 6453. [CrossRef] [PubMed]
16. *DIN EN 843-22006*; DIN 843-2 Advanced Technical Ceramics–Mechanical Properties of Monolithic Ceramics at Room Temperature–Part 2: Determination of Young's Modulus, Shear Modulus and Poisson's Ratio. DIN Deutsches Institut für Normung e.V.: Berlin, Germany, 2006.
17. Munir, Z.A.; Anselmi-Tamburini, U.; Ohyanagi, M. The effect of electric field and pressure on the synthesis and consolidation of materials: A review of the spark plasma sintering method. *J. Mater. Sci.* **2006**, *41*, 763–777. [CrossRef]
18. Foster, L.M.; Long, G.; Hunter, M.S. Reactions Between Aluminum Oxide and Carbon The Al_2O_3—Al4C3 Phase Diagram. *J. Am. Ceram. Soc.* **2006**, *39*, 1–11. [CrossRef]
19. Zienert, T.; Dudczig, S.; Fabrichnaya, O.; Aneziris, C.G. Interface reactions between liquid iron and alumina–carbon refractory filter materials. *Ceram. Int.* **2015**, *41*, 2089–2098. [CrossRef]
20. Fan, Z. A new approach to the electrical resistivity of two-phase composites. *Acta Metall. Mater.* **1995**, *43*, 43–49. [CrossRef]
21. Coto-Ruiz, F.J.; de la Cruz-Blanco, A.; Moriche, R.; Morales-Rodríguez, A.; Poyato, R. Graphene/Zirconia Composites for Components in Solid Oxide Fuel Cells: Microstructure and Electrical Conductivity. *Nanomaterials* **2025**, *15*, 1314. [CrossRef] [PubMed]
22. Smetanina, K.E.; Andreev, P.V.; Nokhrin, A.V.; Lantsev, E.A.; Chuvildeev, V.N. Carbon contamination during spark plasma sintering of powder materials: A brief overview. *J. Alloys Compd.* **2024**, *973*, 172823. [CrossRef]
23. Tokita, M. Progress of Spark Plasma Sintering (SPS) Method, Systems, Ceramics Applications and Industrialization. *Ceramics* **2021**, *4*, 160–198. [CrossRef]
24. Shabalin, I.L. *Ultra-High Temperature Materials I*; Springer: Dordrecht, The Netherlands, 2014. [CrossRef]
25. Kirkpatrick, S. Percolation and Conduction. *Rev. Mod. Phys.* **1973**, *45*, 574–588. [CrossRef]
26. Singh, D.; Agrawal, D.; Chatterjee, A.P.; Kudisonga, C.; Heitzmann, M.T.; Rawal, A. Continuum Percolation in Anisotropic Rectangles: The Role of Excluded Area and Average Connectivity at the Threshold. *Adv. Theory Simul.* **2025**, *8*, e00580. [CrossRef]
27. Berkowitz, B. Analysis of fracture network connectivity using percolation theory. *Math. Geol.* **1995**, *27*, 467–483. [CrossRef]
28. Sanderson, D.J.; Nixon, C.W. Topology, connectivity and percolation in fracture networks. *J. Struct. Geol.* **2018**, *115*, 167–177. [CrossRef]
29. Seifert, G.; Sharba, S.; Raether, F. Simulating percolation in multiphase materials. *Open Ceram.* **2026**, *27*, 100999. [CrossRef]
30. SPRIGGS, R.M. Expression for Effect of Porosity on Elastic Modulus of Polycrystalline Refractory Materials, Particularly Aluminum Oxide. *J. Am. Ceram. Soc.* **1961**, *44*, 628–629. [CrossRef]
31. Dotta, A.L.B.; Serafini, F.L.; Ordoñez, M.F.C.; Machado, I.F.; Farias, M.C.M. Mechanical and tribological properties of spark plasma sintered Nb–Al_2O_3 composites. *Ceram. Int.* **2021**, *47*, 6800–6812. [CrossRef]
32. Günay, G.; Zienert, T.; Endler, D.; Aneziris, C.G.; Biermann, H.; Weidner, A. High-Temperature Compressive Behavior of Refractory Alumina–Niobium Composite Material. *Adv. Eng. Mater.* **2022**, *24*, 2200292. [CrossRef]
33. Weidner, A.; Ranglack-Klemm, Y.; Zienert, T.; Aneziris, C.G.; Biermann, H. Mechanical High-Temperature Properties and Damage Behavior of Coarse-Grained Alumina Refractory Metal Composites. *Materials* **2019**, *12*, 3927. [CrossRef] [PubMed]
34. Sethi, G.; Myers, N.S.; German, R.M. An overview of dynamic compaction in powder metallurgy. *Int. Mater. Rev.* **2013**, *53*, 219–234. [CrossRef]

35. Attia, U.M. Cold-isostatic pressing of metal powders: A review of the technology and recent developments. *Crit. Rev. Solid State Mater. Sci.* **2021**, *46*, 587–610. [CrossRef]
36. Kingery, W.D.; Berg, M. Study of the Initial Stages of Sintering Solids by Viscous Flow, Evaporation-Condensation, and Self-Diffusion. *J. Appl. Phys.* **1955**, *26*, 1205–1212. [CrossRef]
37. Boldin, M.S.; Popov, A.A.; Nokhrin, A.V.; Murashov, A.A.; Shotin, S.V.; Chuvil'deev, V.N.; Tabachkova, N.Y.; Smetanina, K.E. Effect of grain boundary state and grain size on the microstructure and mechanical properties of alumina obtained by SPS: A case of the amorphous layer on particle surface. *Ceram. Int.* **2022**, *48*, 25723–25740. [CrossRef]
38. Weiner, M.; Zienert, T.; Schmidtchen, M.; Hubálková, J.; Aneziris, C.G.; Prahl, U. A New Approach for Sintering Simulation of Irregularly Shaped Powder Particles—Part II: Statistical Powder Modeling. *Adv. Eng. Mater.* **2022**, *24*, 2200443. [CrossRef]
39. Weiner, M.; Schmidtchen, M.; Prahl, U. A New Approach for Sintering Simulation of Irregularly Shaped Powder Particles—Part I: Model Development and Case Studies. *Adv. Eng. Mater.* **2022**, *24*, 2101513. [CrossRef]
40. Averardi, A.; Cola, C.; Zeltmann, S.E.; Gupta, N. Effect of particle size distribution on the packing of powder beds: A critical discussion relevant to additive manufacturing. *Mater. Today Commun.* **2020**, *24*, 100964. [CrossRef]
41. Munro, R.G. Evaluated Material Properties for a Sintered alpha-Alumina. *J. Am. Ceram. Soc.* **2005**, *80*, 1919–1928. [CrossRef]
42. Trzaska, Z.; Collard, C.; Durand, L.; Couret, A.; Chaix, J.M.; Fantozzi, G.; Monchoux, J.P. Spark plasma sintering microscopic mechanisms of metallic systems: Experiments and simulations. *J. Am. Ceram. Soc.* **2018**, *102*, 654–661. [CrossRef]
43. Kellogg, F.; Hofmeister Mock, C. The Effect of Current Pathways on Spark Plasma Sintering. In *Spark Plasma Sintering of Materials*; Springer: Cham, Switzerland, 2019; pp. 61–92.
44. Vanmeensel, K.; Laptev, A.; Van der Biest, O.; Vleugels, J. Field assisted sintering of electro-conductive ZrO_2-based composites. *J. Eur. Ceram. Soc.* **2007**, *27*, 979–985. [CrossRef]
45. Demuynck, M.; Erauw, J.-P.; Van Der Biest, O.; Delannay, F.; Cambier, F. Influence of conductive secondary phase on thermal gradients development during Spark Plasma Sintering (SPS) of ceramic composites. *Ceram. Int.* **2016**, *42*, 17990–17996. [CrossRef]
46. Jing, X.; Zhao, W.; Lan, L. The effect of particle size on electric conducting percolation threshold in polymer/conducting particle composites. *J. Mater. Sci. Lett.* **2000**, *19*, 377–379. [CrossRef]
47. Sichel, E.K.; Gittleman, J.I.; Sheng, P. Electrical properties of carbon-polymer composites. *J. Electron. Mater.* **1982**, *11*, 699–747. [CrossRef]
48. Sheng, P.; Sichel, E.K.; Gittleman, J.I. Fluctuation-Induced Tunneling Conduction in Carbon-Polyvinylchloride Composites. *Phys. Rev. Lett.* **1978**, *40*, 1197–1200. [CrossRef]